Predicting micromechanical properties of cement paste from backscattered electron (BSE) images by computer vision

Liang, Minfei; He, Shan; Gan, Yidong; Zhang, Hongzhi; Chang, Ze; Schlangen, Erik; Šavija, Branko

DOI
10.1016/j.matdes.2023.111905

Publication date
2023

Document Version
Final published version

Published in
Materials and Design

Citation (APA)
Liang, M., He, S., Gan, Y., Zhang, H., Chang, Z., Schlangen, E., & Šavija, B. (2023). Predicting micromechanical properties of cement paste from backscattered electron (BSE) images by computer vision. *Materials and Design*, *229*, Article 111905. https://doi.org/10.1016/j.matdes.2023.111905

Materials & Design 229 (2023) 111905

Contents lists available at ScienceDirect

Materials & Design

journal homepage: www.elsevier.com/locate/matdes

Predicting micromechanical properties of cement paste from backscattered electron (BSE) images by computer vision

Minfei Liang [a], Shan He [a,*], Yidong Gan [b], Hongzhi Zhang [c], Ze Chang [a], Erik Schlangen [a], Branko Šavija [a]

[a] Faculty of Civil Engineering and Geosciences, Delft University of Technology, Delft 2628 CN, the Netherlands
[b] School of Civil and Hydraulic Engineering, Huazhong University of Science and Technology, Wuhan 430074, China
[c] School of Qilu Transportation, Shandong University, Jinan 250100, China

HIGHLIGHTS

- A Residual Convolutional Neural Network (Res-Net) model was employed to predict indentation modulus and hardness of cement paste from BSE images.
- A dataset comprising 40,000 nanoindentation results and 40,000 BSE images was built to train the model.
- The resulting Res-Net model can precisely predict the elastic modulus and hardness with a R2 of 0.85 and 0.88.
- Deconvolution of Res-Net prediction obtains similar invariant statistics as tested by experiments, which gives strong evidence of the applicability of the Res-Net model.

GRAPHICAL ABSTRACT

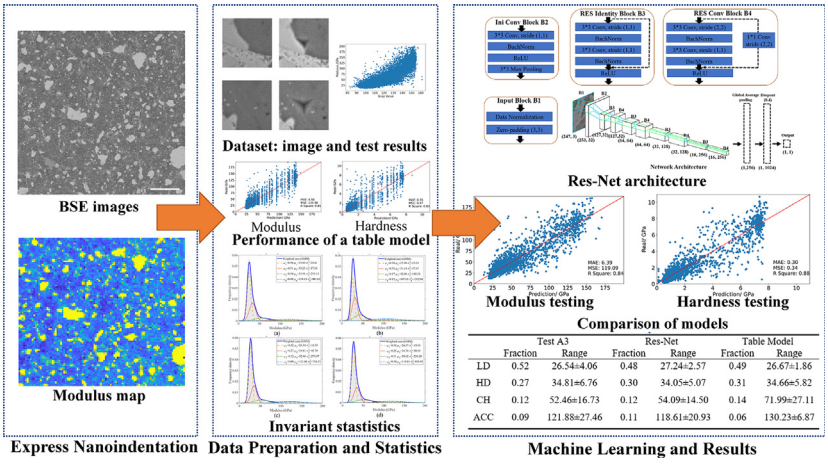

ARTICLE INFO

Article history:
Received 30 October 2022
Revised 20 March 2023
Accepted 1 April 2023
Available online 07 April 2023

Keywords:
Express nanoindentation test
BSE
Cement paste
Computer vision
Res-Net
Elastic modulus
Hardness

ABSTRACT

This paper employs computer vision techniques to predict the micromechanical properties (*i.e.*, elastic modulus and hardness) of cement paste based on an input of Backscattered Electron (BSE) images. A dataset comprising 40,000 nanoindentation tests and 40,000 BSE micrographs was built by express nanoindentation test and Scanning Electron Microscopy (SEM). A Residual Convolutional Neural Network (Res-Net) model, which differs from a typical Convolutional Neural Network (CNN) architecture by a shortcut connection, was employed and compared with a simple table model. The models were trained, tuned, and tested over a training, validation and testing set comprising 70%, 15% and 15% of the 40,000 data pairs, respectively. The following conclusions were drawn: 1) Express nanoindentation tests can provide reliable information for cement paste. Deconvolution based on Gaussian Mixture Model (GMM) can obtain almost invariant statistics for each phase; 2) Based on averaged greyscale values of each BSE image, a table model can predict the elastic modulus and hardness with R^2 of 0.80 and 0.83, respectively; 3) Based on the intensity of each pixel as well as their patterns in each BSE image, the Res-Net model can predict the elastic modulus and hardness with a R^2 of 0.85 and 0.88, respectively. Deconvolution of the Res-Net prediction obtains similar invariant statistics as derived by the nanoindentation tests, which gives strong evidence of the applicability of the Res-Net model.

* Corresponding author.
E-mail address: S.He-2@tudelft.nl (S. He).

https://doi.org/10.1016/j.matdes.2023.111905
0264-1275/

1. Introduction

Hydrated cement paste, as the main binding phase of cement-based materials, forms the basis of the performance of concrete. Mechanical properties of cement paste can provide input parameters for various numerical or analytical models for predicting and analyzing the performance of concrete [1]. In numerical micromechanical modelling, such as the Delft Lattice Model [2], cement paste as a heterogeneous material is often simplified as a multi-phase composite material for the prediction of it the overall mechanical performance, such as uniaxial compressive strength [3], fracture analysis [4], tensile splitting strength [5], creep [6,7], and fatigue [8]. For analytical approaches, based on assumptions of overall shapes of inclusions, micromechanical homogenization schemes like Mori-Tanaka [9] and Self-Consistent [10] are often used to predict the overall mechanical performance of concrete, such as elastic modulus [11–13] and creep [14,15]. Understanding and quantifying the micromechanical properties of cement paste is crucial for understanding and predicting the mechanical properties of concrete.

Nanoindentation is a commonly used technique to probe the micromechanical properties of cement paste. By statistical approaches (*e.g.*, Gaussian Mixture Model and K-means), the histogram of the results of grid-indentation tests can be decomposed into several phases, typically including the anhydrous cement clinker (ACC), calcium hydroxide (CH) and calcium silicate hydrate (CSH), which can be further classified into high-density CSH (HD-CSH) and low-density CSH (LD-CSH) [11]. Combining Statistical Nanoindentation (SNI) with techniques like Energy Dispersion Spectroscopy (EDS) and Backscattered Electron imaging (BSE), mechanical performance of the heterogeneous cement paste can be qualitatively explained by microstructures and chemical compositions. Sorelli et al [16] conducted SNI on Ultra High Performance Concrete by combining SNI, SEM and X-ray Diffraction (XRD), and built a four-level micromechanical model. Vandamme et al [14] tested the creep properties of CSH on different cement pastes and captured the creep compliance of CSH by a logarithmic time function. Hu and Li [17] combined SNI and SEM to test the micromechanical properties of Portland cement paste and used the elastic modulus of different phases to predict the elastic modulus on the macroscale using a homogenization method. Similarly, Da Silva et al [18] conducted SNI on high performance cementitious composites and obtained the elastic modulus of each single phase. Through a two-step analytical homogenization scheme, they used the SNI testing results as input and successfully predicted the elastic modulus tested at the macroscale. Overall, SNI-based methods have proven to be sound and effective in a number of studies on micromechanical properties of different cementitious materials, including elastic modulus of blended cement pastes [19], polymer-modified cement pastes [20], geopolymers [21,22], seawater-mixed alite paste [23], nature pozzolan concrete [24] and creep properties of Portland cement paste [25,26].

Despite the prevalence and usefulness of the SNI-based approaches, limitations still exist. The most inherent limitation is the assumption that the cement paste only has a certain number of homogeneous phases. Although it is a reasonable simplification, it neglects the variance of the properties of each phase and takes only the average values into account. However, during each nanoindentation test, it is actually a cluster of composite phases that are being indented [27,28]. Large variations of elastic modulus of CSH have also been reported [29]. Instead of assuming only a few numbers of phases exist, a much better solution would be to use the correlation between greyscale values and tested modulus (or hardness) directly, without doing any deconvolution into a few phases. This is for instance done in our previous studies [30,31]. However, since most modelling tools need such a deconvolution and comparing statistics is easier, the method of deconvolution in four phases is also done in this paper. The second limitation of SNI lies in the efficiency of nanoindentation tests and the potential influence of data number on the deconvolution results. Since cement paste is highly heterogeneous, statistical deconvolution procedure requires a considerable amount of data to obtain an accurate result of phase fraction, (average) micromechanical properties and variance. In most SNI studies mentioned above, the number of indents used for deconvolution typically lies between 100 and 500. The philosophy behind for the determination of a proper indentation number seems unclear. The final limitation of SNI is the availability of the testing facility itself. Because of its high requirement on the lab condition, a Nanoindenter is not widely available, which may also hinder the research of micromechanical properties of cementitious materials.

In view of these limitation, an effective way to overcome them would be to develop a correlation model directly from the microstructure to the micromechanical properties. The difficulty of building such a model lies in the complexity and randomness of microstructure of cement paste. In the authors' previous studies [30,31], based on histogram analysis, it was proven that the greyscale values from X-ray computed tomography (XCT) can be linearly correlated with the elastic modulus measured by nanoindentation. The underlying mechanism of this correlation is that the greyscale values of XCT stand for the density function [32], while the density is closely related to the mechanical properties [33]. Meanwhile, the depth of the nanoindentation was set such that it would probe the volume approximately equal to the size of a single voxel for XCT. However, the simple table model does not reflect the microstructural effects (*e.g.*, shapes, distributions and heterogeneity of various phases) and therefore the prediction accuracy is limited. On the other hand, the high heterogeneity of real microstructure of cement paste also hinders the application of a pure analytical approach from building a correlation model between the microstructural input and micromechanical properties.

This study aims to deal with the complexity of cement paste by data-driven models. BSE image, whose brightness in greyscale is primarily a function of the atomic number of the atoms [34], will be used to represent the local microstructure of the material probed by nanoindentation. A computer vision model is developed to map the micromechanical properties with the microstructure images as input. The application of Convolutional Neural Networks (CNN) has prevailed in many modern image recognition and object detection tasks. In the field of civil engineering, CNN has been proved to be an effective tool for crack detection [35–38], structural health monitoring [39,40] and post-disaster inspection [41]. Moreover, CNN also showed excellent performance in homogenization of mechanical properties and behaviors of various composite materials, such as the stress–strain curves of composite microstructures [42], elastic modulus and Poisson ratios of randomly-generated heterogeneous microstructures [43], and creep modulus of cement paste based on X-ray tomography scans and Lattice model [44]. Recently, Hilloulin et al [45,46] built segmentation models with Mask R-CNN for identifying and segmenting the air voids and aggregate in microscopic images of concrete.

In this study, a Residual Convolutional Neural Network (ResNet), which differs from CNN by shortcut connections, was built for predicting the micromechanical properties (*i.e.*, elastic modulus and hardness) of a given microstructure. Express nanoindentation tests was conducted to generate a large number (*i.e.*, 40,000) indentation results (comprising indentation elastic modulus and hardness for each data point). At the locations where the indents were made, 40,000 BSE images were taken at a resolution of

247 × 247 pixels over regions of 10 μm by 10 μm (40 nm/pixel). The 40,000 BSE images and 40,000 indentation results (*i.e.*, elastic modulus and hardness) form the dataset for training the Res-Net. This paper is organized as follows: Section 2 introduces the experimental details of nanoindentation tests and BSE image acquisition. Section 3 shows how the dataset for training the Res-Net is built. Section 4 briefly introduces the basics of CNN, the designed architecture of the adopted Res-Net, and the training process. Section 5 gives the statistical characteristics of the dataset and evaluates the performance of the built Res-Net.

2. Experimental programs

The experimental part of the current study aims to build a dataset of BSE micrographs and nanoindentation test results for the training and testing of the Res-Net model. BSE imaging were performed by a Scanning Electron Microscopy (SEM) with automated acquisition function over an identical area (2.7 × 3.4 mm^2) 2 times, both before and after the indentation test. The images taken before the nanoindentation tests were used as model input, while the images taken after the indentation test was used to locate the exact position of each indent. A micro-positioning procedure was implemented to crop out 40,000 BSE images (individual image size = 1 0 μm × 10 μm) corresponding to the 40,000 indents, which then form the whole dataset.

2.1. Sample preparation

In this study, CEM I 52.5 N Portland cement was used to prepare a cement paste with a w/c of 0.4. After casting, the sample was cured at a constant room temperature of 20 ± 3 degrees for 28 days. Afterward, the hydration of the cement paste was stopped by using the solvent exchange method with isopropanol [47]. After the hydration was stopped, the sample was sliced into thin plate-like specimens of 1.5 mm thick by a micro-dicing saw. The use of a micro-dicing saw is to ensure that the top and bottom surfaces of the sample are parallel. Afterward, the sample was first ground by 4000 grit abrasive papers for 5 min and then polished with a synthetic silk polishing cloth (MD-Dac from Struers) charged with 3 μm and 1 μm diamond paste for 2 separate 30-minute sessions. An oil-based lubricant (DP-Lubricant Brown from Struers) was used to dissipate any heat built-up. Between each grinding/polishing interval, the sample was immersed in an ultrasonic bath for 30 s to remove debris from the surface. Following the procedure introduced above, a mirror-like surface which can reflect the overhead light was obtained, as shown in the Fig. 1. Previous study [48] suggested a criterion based on root-mean-squared (RMS) roughness to evaluate the surface finishing for nanoindentation test. However, they also noted that the calculation of RMS is largely influenced by the data processing method as adopted in a specific Atomic Force Microscopy (AFM). A more convenient rule-of-thumb to evaluate surface finishing would be to see if the surface can be mirror-like and reflect overhead light.

2.2. BSE images

The BSE images were taken by a FEI QUANTA FEG 650 SEM at an accelerating voltage of 15 kV. Before the BSE imaging, the sample was coated with a layer of carbon having a thickness of roughly 10 nm. Within the entire area of interest, a 40 × 40 tile set was first prescribed; and the BSE images were taken automatically with a commercial software (Maps 3 from Thermo Fisher Scientific) at a nominal magnification of 5,000×. The images were then electronically stitched to a single image (2.7 × 3.4 mm^2) as shown in Fig. 2. The resolution of final BSE image of the area is 40 nm/pixel. Four areas (A1-A4 as shown in the Fig. 2) were selected for dataset acquisition. The sizes of A1-A4 are 1 × 1 mm^2, 1 × 1 mm^2, 2 × 1 mm^2, 2.6 × 0.7 mm^2, respectively. Express nanoindentation tests were used on the areas A1-A3, which contained 10,000, 10,000, and 20,000 indents, respectively. Nanoindentation results of A1-A3 formed the dataset for training and testing the Res-Net. Note that there were no nanoindentation tests being performed on the area A4. The area A4 was selected for out-of-bag test based on the invariant deconvolution statistics derived from the results of A1-A3 (see Section 5.1). After nanoindentation tests, the BSE images of the areas A1-A3 containing indentation marks were acquired and used as reference in the micro-positioning procedure, which will be described in the section 3.2.

2.3. Statistical express nanoindentation

In most SNI studies, nanoindentation tests were performed by either load-controlled methods or the Continuous Stiffness Measurement (CSM) method. Each indentation test performed with these methods normally takes 6–10 min. Indentations of a large array are usually very time-consuming. To solve this issue, this study carried out high-speed nanoindentation tests using the KLA G200 nanoindenter equipped with a Dynamic Contact Module II (DCM II) head and a diamond Berkovich tip, which allow the options of both express test and CSM. This improvement in testing efficiency provides the possibility for building the data-driven model of the current study. It was also proven that the express test greatly improves the stability of deconvolution results [49].

During the express nanoindentation test, performing each indentation takes only a few second. This testing speed is significantly faster than conventional nanoindentation tests, which usually take several minutes for each indentation. The time-dependent thermal drift is thus considered to be negligible for express nanoindentation test due to the relatively short duration for each test. Nevertheless, this study still measured thermal drift before each batch of tests (with 400 indents in each batch), and only when the thermal drift was lower than 0.05 nm/s could the batch of tests be started. Prior to the test, the tip area function was first cali-

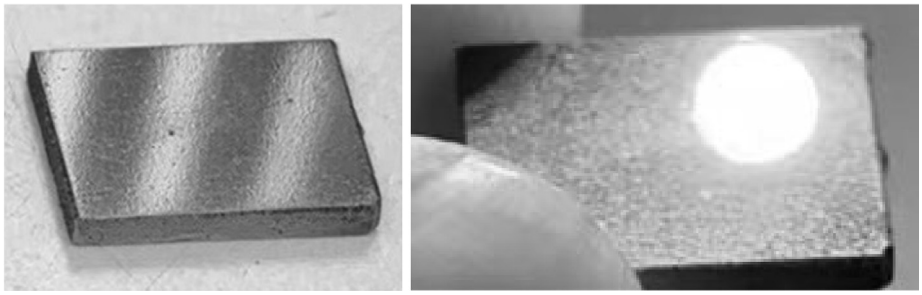

Fig. 1. Photograph showing the reflective sample surface after the polishing process.

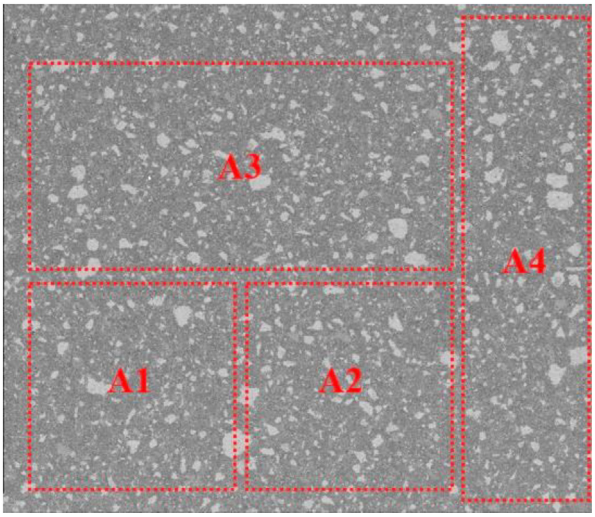

Fig. 2. Prescribed area for dataset acquisition (width of field = 3.4 mm).

brated with a fused quartz reference sample. During the test, the elastic modulus and hardness of the indented material were calculated by the Oliver and Pharr method by fitting the unloading part of the load–displacement curve [50].

For the prescribed areas A1-A3 as mentioned in section 2.2, indentation arrays with sizes of 100 × 100, 100 × 100, and 200 × 100, respectively, were performed. The indentation depth was set to 500 nm and the spacing was set to 10 μm. In each array, indentation tests were conducted in batches, with each batch containing 20 × 20 indents. The reason for separating the big array in batches is to prevent the accumulation of errors when locating indents. In each batch, the nanoindenter first conducts surface approaching and drift correction and then moves to the next indent by the specified spacing distance (*i.e.*, 10 μm). However, deviation of indent spacing and depth from prescribed values often happens, which was also observed in [49]. This study chose to do the big array test in batches so that the error of indentation location can be reset at the beginning of each batch.

3. Data preprocessing and analysis

3.1. Gaussian Mixture model for statistical deconvolution

As a highly heterogeneous material, the micromechanical properties of cement paste vary widely due to 1) the presence of randomly distributed irregular-shaped hydration products; and 2) the variability in chemical compositions of different hydration products. Therefore, statistical approaches are usually needed when dealing with grid-indentation results. This paper adopts the Gaussian Mixture Model (GMM) to decompose the probabilistic distribution of micromechanical properties of each single phase from the overall histogram of the testing results, under the following assumptions: 1) the distribution of each single phase follows Gaussian Distribution; and 2) the superposition of the distribution of different phases are linear. In the GMM model, the overall distribution of testing results (X) can be expressed as the weighted sum of the distribution of multiple phases X_i (i = 1,2,3,. . .,N), as below:

$$p(X|\{w,\mu,\sigma^2\}) = \sum_{i=1}^{N} w_i p(X_i|\{\mu_i,\sigma_i^2\}) \tag{1}$$

where w_i, X_i, μ_i, σ_i are the fraction, probabilistic distribution function, mean, and standard deviation of i-th single phase, respectively. The probabilistic distribution X_i is a Gaussian distribution and, therefore, is solely determined by its mean and standard deviation, as below

$$p\left(X_i|\left\{\mu_j,\sigma_j^2\right\}\right) = \frac{1}{\sqrt{2\pi\sigma_i^2}} exp\left(\frac{(X_i-\mu_i)^2}{2\sigma_i^2}\right) \tag{2}$$

3.2. BSE micro-positioning

The aim of micro-positioning is to compensate for the movement error of the indenter in each batch (20 × 20 array) and to locate the 40,000 indents. Taking area A1 as an example (Fig. 3 **left**), a sliding window with the size 210 μm × 210 μm scans over every batch. Within each batch, two components are needed to determine the locations of the 400 indents: 1) the coordinate of the first indent O (x_0, y_0) of each batch (bottom-left indent in Fig. 3 **middle**); and 2) Δx_j and Δy_i representing the movement error along the x-axis and y-axis at column j and row i respectively (Fig. 3 **right**). The coordinate of any indents ($x_{i,j}$, $y_{i,j}$) can be calculated as follows:

$$x_{i,j} = x_0 + \sum_{k=1}^{j-1} \Delta x_k \tag{3a}$$

$$y_{i,j} = y_0 + \sum_{k=1}^{i-1} \Delta y_k \tag{3b}$$

where i, j = 1, 2, 3,. . ., 20, represent the row and column indexes of the indents in every single batch. Both Δx_j and Δy_i were specified as 0.05 μm at the beginning and needed fine-tuning for each column and row, respectively.

After the locations of all 40,000 indents were found in the BSE image taken after the nanoindentation test, the BSE image taken before the tests was overlapped on it. The 40,000 rectangular BSE images with a size of 10 μm × 10 μm corresponding to each indent were then cropped from the BSE image before the tests. The overall procedure of micro-positioning is shown in the Fig. 4. Examples of cropped images before and after the tests are shown in Fig. 5. Good accuracy of micro-positioning procedure can be found by comparing the BSE images taken before the tests (Fig. 5 **left**) and those after the tests (Fig. 5 **right**).

4. Computer vision

4.1. Convolutional Neural network (CNN) overview

CNN is a major technique in the field of Computer Vision, which aims to extract high-level information from digital images or videos [51]. A CNN typically includes the following layers: a convolutional layer, an activation layer, and a pooling layer [52]. A convolutional layer works by sliding a filter (the so-called kernel), typically with the size 3 × 3, 5 × 5, or 7 × 7, over the input image (or feature map), and extract the local features by element-wise multiplication, expressed as below:

$$y_{i+1}^j = \sum_k w_{ik}^j x_i^j + b_i^j \tag{4}$$

where i, j, k are the indices of layers, channels and filter elements, respectively; x and y are elements of input and output tensors of each convolutional layer; w and b are learnable parameters of the filter, which are typically updated by gradient descent in each learning iteration. Following the convolutional layer, an activation function is attached to add nonlinearity. In this study, the rectified linear unit (ReLU) was used, which excludes all negative input, and can be expressed as below:

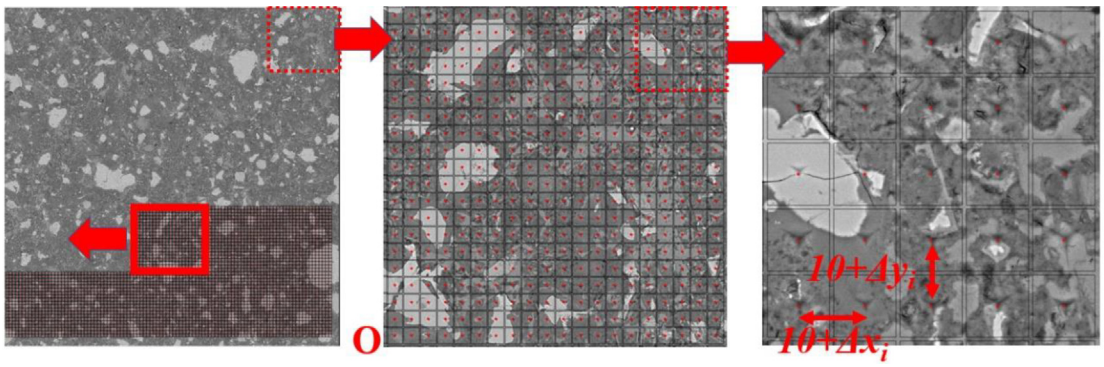

Fig. 3. Indent array and modulus map (left: indent array A1; middle: the last batch of nanoindentation tests in array A2; right: random cropped positioning results).

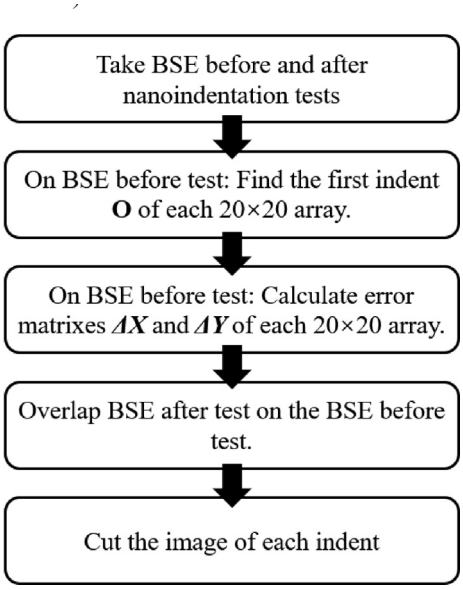

Fig. 4. Micro-positioning workflow.

$$f(x) = \begin{cases} xx \geq 0 \\ 0x < 0 \end{cases} \quad (5)$$

Finally, for typical CNN architectures, a pooling layer is often attached after the activation layer to achieve down sampling, which highly benefits the computational efficiency and removes features that are of less importance to increase the model robustness. The pooling layer works by replacing the output at a certain location of the input with a summary statistic of the nearby outputs. This study used max-pooling, which preserves the maximum value of a rectangular neighborhood. On the other hand, another option to achieve the down sampling is by setting a higher stride of the filter in the convolutional layer. Compared with the pooling layers which are fixed operations, down sampling through a higher stride embeds the pooling procedure in the convolutional layer and thus is controlled by the learnable parameters of the filter. Therefore, increasing stride is expected to improve the expressiveness capability and prediction performance [53]. In this study, most of the down sampling procedures were achieved by a stride of 2 in the convolutional process.

Except for typical CNN layers, the backbone of the adopted network architecture is the residual deep learning with shortcut connection introduced by He et al. [54], which effectively solves the problems of gradient vanishing/ explosion and degradation for deep networks. A schematic diagram of the residual learning is shown in the Fig. 6. Assuming the objective mapping as *H(x)* and the mapping represented by the deep learning neural network is *F(x)*, normally the learnable parameters in the neural network will be optimized to force *F(x)* to approach *H(x)* by algorithms like gradient descent, as shown in Fig. 6a. While with a shortcut connection of identity mapping, the objective of *F(x)* becomes the residual mapping *F(x):=H(x)-x*, which is easier to optimize compared with the original mapping *F(x):=H(x)*.

4.2. Network architecture

This study adopted a network architecture as shown in Fig. 7, which resembled the network architecture of ResNet-18 in [54].

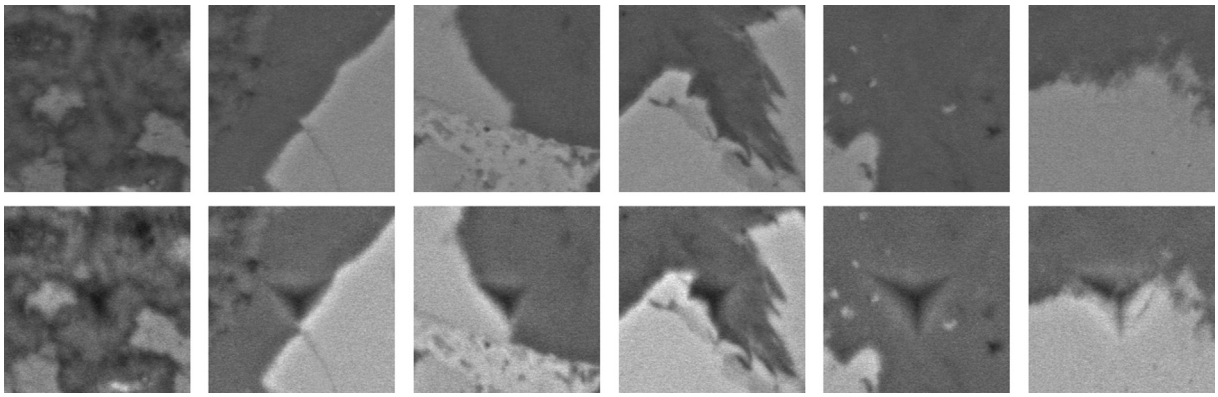

Fig. 5. Randomly selected micro-positioning results (left: BSE images before nanoindentation; right: BSE images after nanoindentation). Each BSE image has 247 pixel × 247 pixel and represents an area of 10 μm × 10 μm.

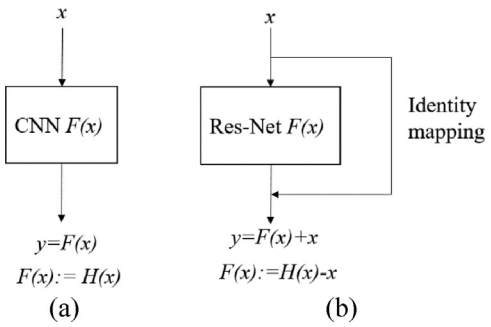

Fig. 6. Schematic diagrams of (a) CNN block and (b) Residual block [54].

Four types of blocks exist in the Res-Net of this study, including the input block B1, initial convolution block B2, residual identity block B3, and residual convolution block B4. The blocks B1 and B2 are first stacked in sequence; and then blocks B3 and B4 are stacked iteratively for 3 times. A batch normalization layer is attached after every convolution layer to ensure stable convergence and to prevent gradient vanishing/explosion. In the input block B1, the image tensor is firstly normalized by its mean and variance; and then zero values will be used to expand the dimension of the image tensor by 6 (3 at each edge) so as to prevent information loss when the filter reaches the edge. The initial convolution block B2 is a typical CNN block based on a convolution layer with 3 × 3 filter moving by a stride of 1. The blocks B3 and B4 are the residual learning blocks and serve as the backbone of this Res-Net model. Both B3 and B4 contain two consecutive convolutional layers, which can effectively expand the receptive field. The shortcut connection in B3 is an identity mapping. It should be noted that no pooling layers are need in blocks after B2. In B4, the first convolution layer moves the filter by a stride of 2, which achieves the aim of down-sampling, as explained in the section 4.1. To keep the size of input and output the same, the shortcut connection of B4 is a convolution layer with a 1 × 1 filter size and a stride of 2. Finally, a global average pooling layer is attached after the last B4 and the average of each channel in the feature map of B4 is calculated and stored in a 1 × 256 vector. A hidden layer with 1024 neurons with a dropout rate of 0.4 is used to map the 1 × 256 vector to a 1 × 1 vector, which is the prediction objective (*i.e.*, elastic modulus or hardness). In total, the Res-Net built herein contains 3,060,161 trainable parameters and 3904 non-trainable ones.

4.3. Training strategies

In the training process, the 40,000 samples (including 40,000 BSE images and 40,000 nanoindentation results) were randomly divided into a training set, a validation set, and a testing set, with a ratio of 7: 1.5: 1.5. Thereby, 28,000 samples were located in the training set; 6,000 samples were located in the validation set; and 6,000 samples were in the testing set. The nanoindentation results (*i.e.*, elastic modulus and hardness) were normalized by their mean and variance before they were used for training. The training set was used to train the model by gradient descent. Mean squared error (MSE) was used as the loss function to implement the gradient descent to back propagate the error and to optimize the learnable parameters of the Res-Net. The Adaptive Moment Estimation (Adam) algorithm [55] was used for the gradient descent process. The Adam algorithm contains two momentum terms to preserve the historical values of gradient and can therefore avoid local minima. This study also adopts an adaptive exponential-decay approach to update the learning rate: for every five epochs, if the prediction performance of the validation set is not improved, the learning rate will be decayed by a proportion of 0.9. By comparing the prediction performance of the Res-Net on the validation set, the initial learning rate was tuned as 1.0×10^{-5} and the batch size of the training process was set as 32. In total, 100 epochs were used for the training process and the model obtained best performance in the validation set was selected.

After the training process, the model that obtained the best performance on the validation set was selected. Afterwards, the selected model made predictions on the testing set, which was kept isolated until the end of training. Mean Squared Error (MSE), Mean Absolute Error (MAE), and Coefficient of Correlation (R^2) were used as the metrics to evaluate the prediction performance, as below:

$$MSE = \frac{1}{n}\sum_{i=1}^{n}(y_i - \hat{y})^2 \tag{6}$$

$$MAE = \frac{1}{n}\sum_{i=1}^{n}|y_i - \hat{y}| \tag{7}$$

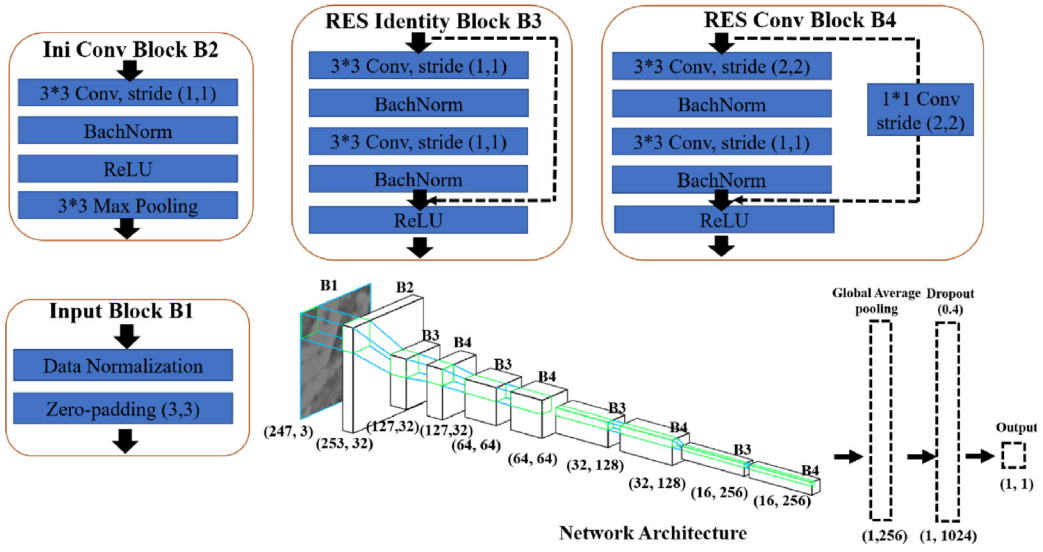

Fig. 7. Illustration of the architecture of Res-Net.

$$R^2 = 1 - \frac{\sum_{i=1}^{n}(y_i - \hat{y})^2}{\sum_{i=1}^{n}(y_i - \bar{y})^2} \quad (8)$$

5. Results and discussion

5.1. Database overview

Since elastic modulus has a strong linear correlation with hardness [56,57], only the nanoindentation results of elastic modulus will be analyzed in detail. The overall BSE images of the 40,000 indents in areas A1, A2, and A3 (specified in section 2.2) are shown in the Fig. 8 **(a, c, e)**. The nanoindentation results of elastic modulus corresponding to these three areas are shown in Fig. 8 **(b, d, f)**. The distribution of elastic modulus shows strong correlations with the BSE images. Identical shape and distribution of ACC can be found in the BSE images (*i.e.*, light grey particles) and the elastic modulus maps (*i.e.*, yellow areas). Other phases are less discriminative in the BSE images, but in the modulus map the overall patterns of phase distributions (segmented by the GMM deconvolution results in Fig. 9) are clearer: the ACC (*i.e.*, yellow area where elastic modulus is approximately higher than 80 GPa) is surrounded by CH and HD-CSH (*i.e.*, green area where elastic modulus is approximately higher than 35 GPa). The LD-CSH (*i.e.*, blue area where elastic modulus is approximately lower than 35 GPa) forms the matrix which occupies the highest proportion of the cement paste composite.

The histograms of elastic modulus measured by the nanoindentation tests over the areas A1, A2, A3, and their sum are shown by the grey bars in Fig. 9. There are 10,000, 10,000, and 20,000 indents in the areas A1, A2, A3 respectively. GMM was used to decompose the overall histogram under the assumption that the cement paste can be viewed as a four-phase composite at the microscale. The blue solid line in the Fig. 9 is the weighted sum of the distribution of the four phases, which corresponds to the theoretical histogram of the elastic modulus results. A good match between the theoretical histogram (blue solid line) and the real histogram (gray part) indicates that good accuracy of the GMM deconvolution. The ω, μ, and σ represent the fraction, mean, and variance of each individual phase, respectively. Indices 1, 2, 3, 4 represent the phase LD-CSH, HD-CSH, CH, and ACC, respectively. The results in Fig. 9 support the following findings:

1) The GMM deconvolution, assuming four phases are present in hydrated cement paste, shows good accuracy, since the theoretical histogram coincides well with the real histogram.
2) The deconvolution results of testing areas A1 (10,000 indents), A3 (20,000 indents) and A1 + A2 + A3 (40,000 indents) are consistent: highly similar values of fraction, mean, and variance for each phase were obtained. The GMM deconvolution results show that the statistical deconvolution has invariant statistical characteristics which may reflect the inherent hydration status of cement paste. Following Jenning's model of two-type CSH [58], the hydration degree α and ratio between HD-CSH and LD-CSH M_r of the cement paste can be estimated following the formulas below:

$$\alpha = \frac{\frac{V_h}{V}}{\frac{V_h}{V} + V_a} \quad (9)$$

$$M_r = 3.017\left(\frac{w}{c}\right)\alpha - 1.347\alpha + 0.538 \quad (10)$$

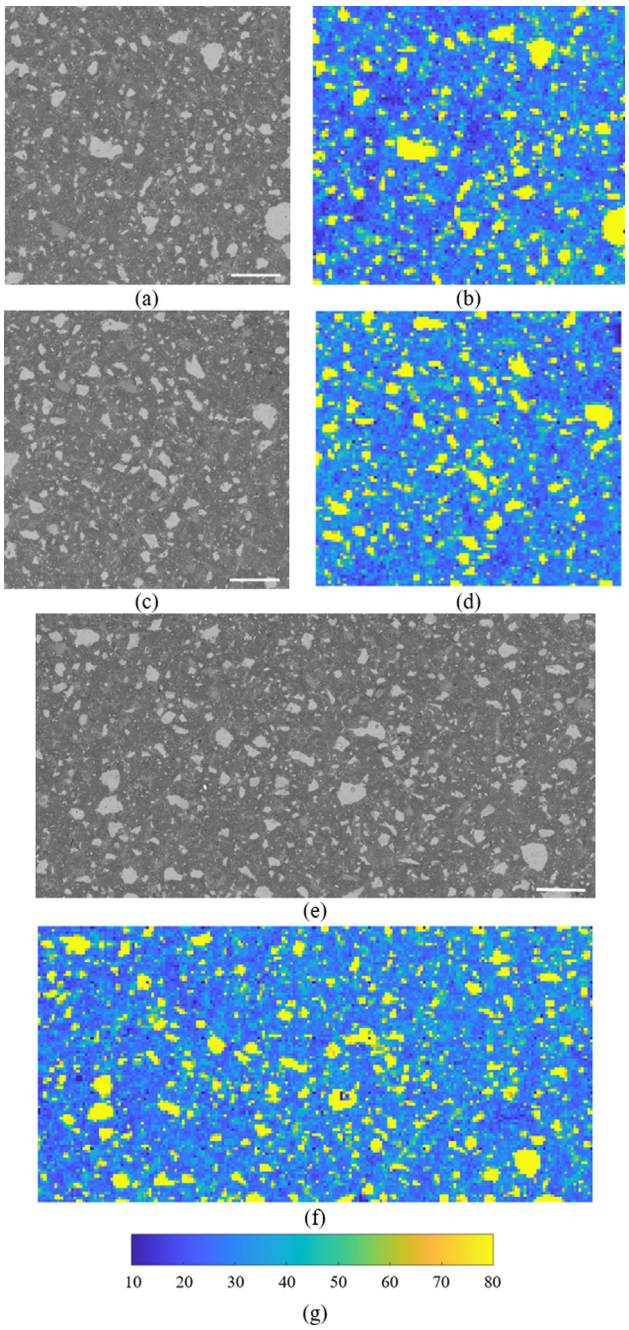

Fig. 8. Indent array and modulus map (a, c, e and b, d, f are BSE images and modulus maps of indent arrays A1, A2 and A3; g is the legend of modulus maps with the unit GPa). Scale bar = 200 μm.

where V_h, V_a are volume fraction of hydration products and the ACC respectively; V is the volume ratio of reaction product to reactant, which can be assumed as 2.2 according to [59]. Based on the deconvolution result of the 40,000 indents in areas A1 + A2 + A3, where the first three phases (*i.e.*, LD-CSH, HD-CSH, CH) correspond to the hydration product and their volume fraction V_h equals to 0.90 and the volume fraction of ACC V_a equals to 0.10, the α and M_r can be calculated according to Eq (9–10) as 0.8036 and 0.4253, respectively. In comparison, the tested M_r is 0.463, which is close to the calculated result. The difference between the calculated and tested M_r may be induced by the assumption of reaction product-reactant volume ratio and difference of clinker compositions.

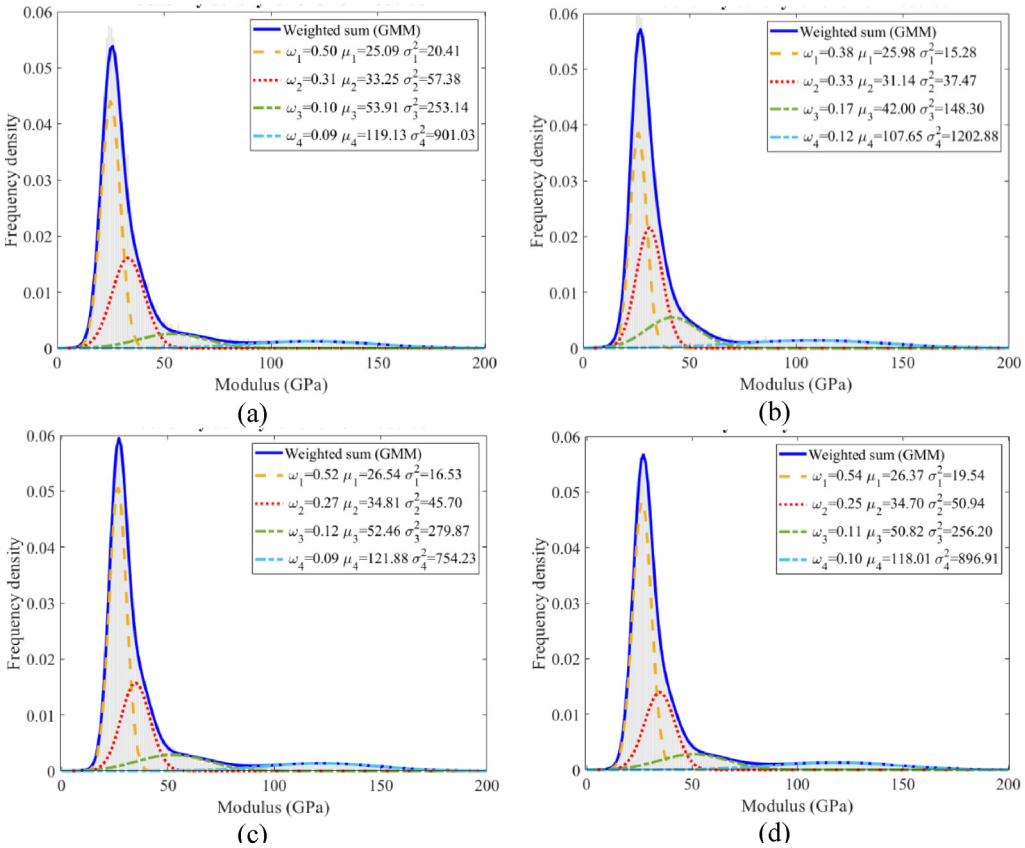

Fig. 9. Indent array and modulus map (a, b, c, d are histograms and deconvolution results of indent arrays A1, A2, A3 and A1 + A2 + A3; The subscript 1, 2, 3, 4 represents the phases of LD-CSH, HD-CSH, CH and ACC respectively.).

3) The deconvolution results of the testing area A2 (10,000 indents) preserves similar average values of LD-CSH and HD-CSH with the other areas. However, considerable inconsistency was found in the values of fractions of two types of CSH and all statistics of CH and ACC. The result here supports the fact that the influence of data number on SNI results is not negligible. It was also reported by [22] that the volume fraction of each phase would be better estimated from BSE images rather than from nanoindentation elastic modulus mapping, which is extracted with a lower resolution because a certain distance is needed between two indents. Regarding the deviation of the CH phase and the ACC phase in the deconvolution results of A2, one possible reason accounting for the inconsistency is that the chemical compositions of those two phases are inherently more complex than CSH. This can be also seen from the high variance value obtained in the results of A1, A3, and A4. Besides, the nanoindentation results of the CH phase also depends on the crystal orientation during testing [60]. Another reason accounting for the instability is the small number of CH and ACC: the two types of CSH occupy around 80% of the cement paste, while the CH and ACC only account for around 20%, which makes less data for CH and ACC and therefore results in variability.

5.2. Correlation between grayscale and modulus: A table model

In the authors' previous study [30,31], it was proven that because the greyscale values of XCT stand for the density function [32], the XCT greyscale values can be linearly correlated with the elastic modulus measured by nanoindentation. In this study, the intensity of the BSEs (and therefore the greyscale value of the BSE images) is a function of the atomic number of the atoms in the area of interest. The average greyscale value of each BSE image indicates a different phase assemblage of the corresponding area, and thus corresponds to different micromechanical properties. Herein, as shown in Fig. 10, the average greyscale value of each 10×10 μm^2 BSE image was correlated with corresponding elastic modulus and hardness tested by nano-indentation. Fig. 10 shows a clear positive correlation between the grayscale values of BSE images and the results of nanoindentation elastic modulus. By splitting the 40,000 dataset into a training set of 32,000 and testing set of 8,000, a linear regression model [61] and a table model were trained and tested to predict the elastic modulus and hardness based on average greyscale values in a 10×10 μm^2 BSE image. Note that a validation set was not necessary here because there is no need for hyperparameter tunning for both linear model and table model. Therefore, a splitting ratio of 8:2 was adopted.

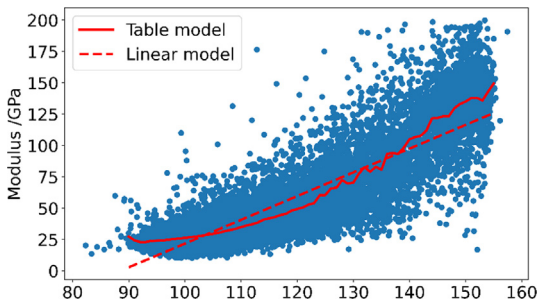

Fig. 10. Correlation between the modulus tested by nanoindentation and average greyscale value of corresponding 10×10 μm^2 BSE image.

The so-called table model is intrinsically a classification model that classifies all the microstructures (*i.e.*, BSE images) according to their different average greyscale values and assign the average elastic modulus tested by nanoindentation to each class of greyscale values. Thereby, a table model includes only two components: 1) average greyscale value; 2) average tested modulus/ hardness corresponding to each average greyscale value. Given a BSE image, the table model works by firstly computing the average greyscale value of the image and then looking up in the table to find the corresponding modulus/ hardness, as shown by the red line in Fig. 10. Because the linear model assumes a linear correlation, while the table model does not make any assumption and only conducts the classification, the performance of the table model significantly outperforms the linear model with a R^2 of 0.80 versus 0.72 in the prediction of elastic modulus. However, as a classification model, the prediction of the table model is not continuous as shown in Fig. 11. Although the table model obtains good prediction performance (quantified by MSE, MAE and R^2) over hardness and elastic modulus, an obvious evenly-distributed error range and non-continuous predictions cannot be neglected. Furthermore, it is clear that the table model fails to predict the modulus at the tail (*i.e.*, modulus with higher values). Such error is understandable since the information contained in an average greyscale value only reflects an approximation of the overall chemical composition, while the microstructural effects (*i.e.*, distribution and shapes) are not accounted.

5.3. RES-Net performance

5.3.1. Training history

A budget of 100 epochs was assigned to train the model of elastic modulus and hardness. The model was trained on a laptop equipped with a GPU Nvidia RTX 3070 with a memory of 6G and the whole training process took approximately 20 min. The training history in Fig. 12 shows the effectiveness of the designed network architecture and hyperparameters: The MAE and MSE of the model on training set decrease rapidly in first 10 epochs and then decreases steadily afterwards. However, the performance of the model on validation set only improves in the first 25 epochs for the modulus model, and the first 16 epochs for the hardness model. Afterwards, further epochs only result in improvement in the training set and do nothing good for the validation set, meaning that overfitting occurs. Therefore, the model that was trained at 25th epoch and 16th epoch was selected as the modulus model and hardness model, respectively.

5.3.2. Testing

After the models were trained, they were tested by the 6,000 samples in the testing set. The prediction performance of the Res-Net on the testing set are shown in the Fig. 13. Both the hardness model and modulus model obtain good prediction performance with a R^2 of 0.85 and 0.88 in the testing set. Thanks to the early-stopping in the training process, the testing performance of both the hardness model and the modulus model in the testing set are only slightly inferior than that on the training set, which ensures no overfitting has occurred. Compared to the table model presented in section 5.2, the Res-Net exhibits improvement in prediction accuracy for both elastic modulus and hardness in training and testing set. Moreover, the predictions made by the Res-Net are more continuous and display smaller error range. This should be attributed to the complexity of models and thus the information extracted from the input: the table model takes the average greyscale value of the $10 \times 10\ \mu m^2$ BSE image as input, which contains only the information of the overall chemical compositions of the composite and thus the table mapping can only obtain limited accuracy. However, the Res-Net extracts information from the entire BSE image by convolution, which contains the microstructural information of the composite that was indented, including the distribution and shapes of different phases. By stacking multiple convolutional layers together, the Res-Net forms a very com-

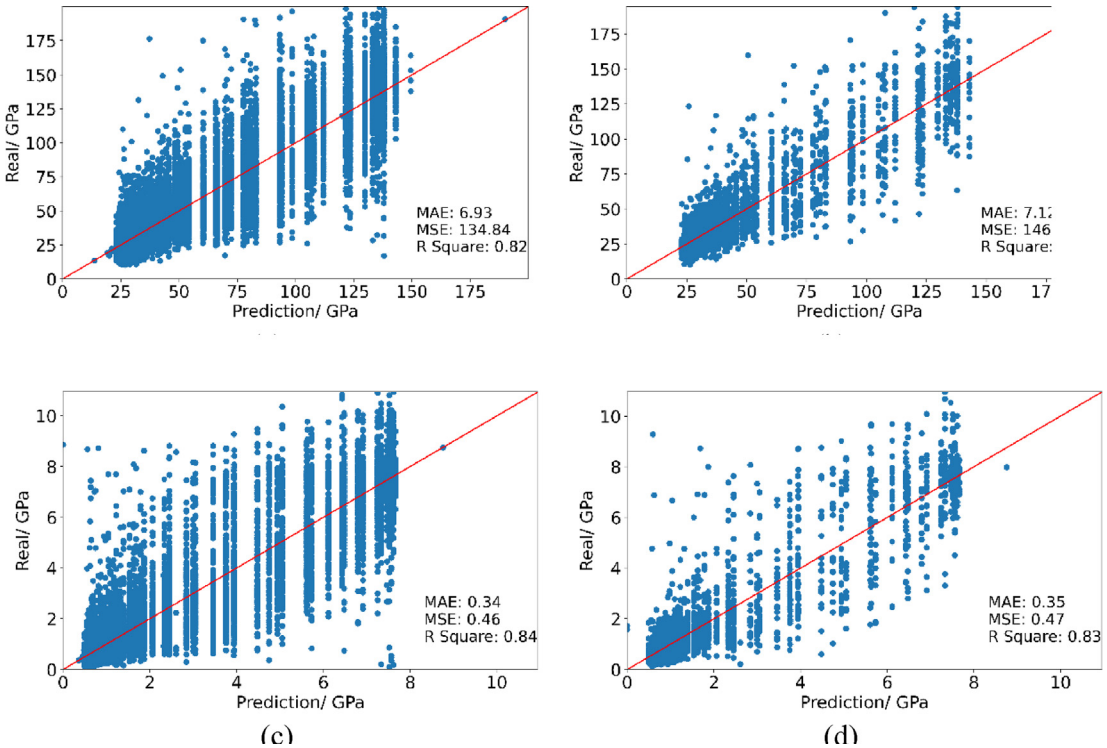

Fig. 11. Table model of modulus given average grayscale value as input (a, b: training and testing set for modulus; c, d: training and testing set for hardness).

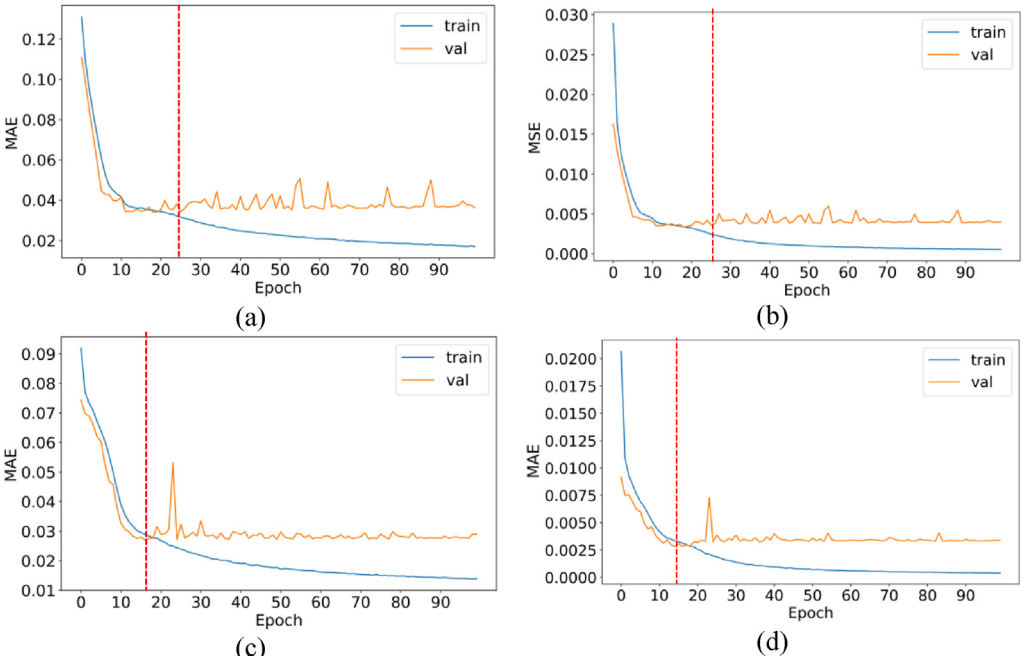

Fig. 12. Res-Net training histories (a, b: Training history of MAE and MSE of modulus model; c, d: Training history of MAE and MSE of hardness model) Note that the numbers in y-axis of are not values of modulus/ hardness, but the normalized values of them.

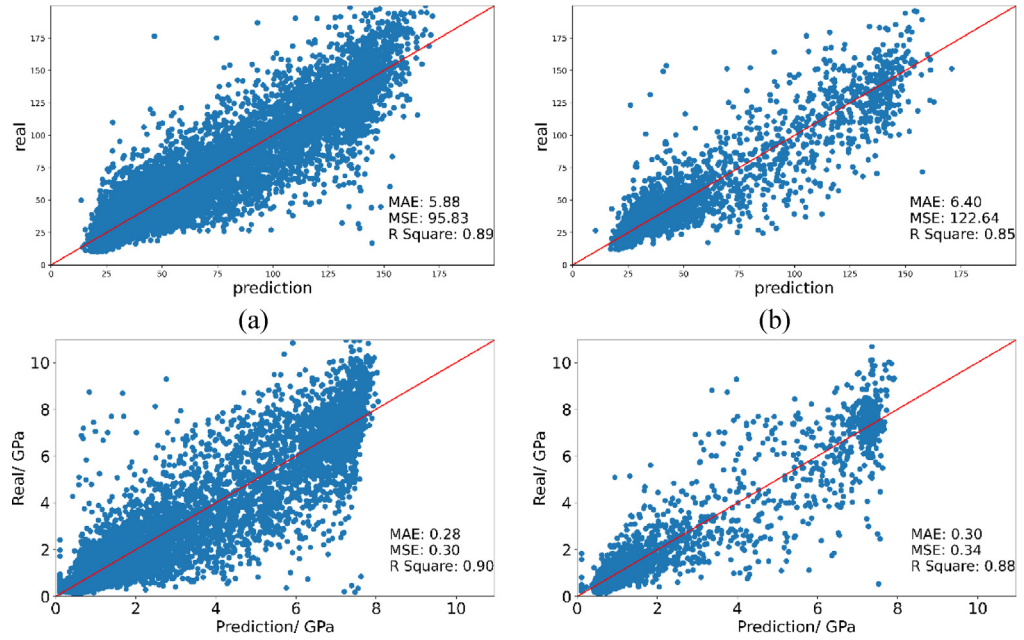

Fig. 13. Performance of Res-Net model of modulus and hardness given BSE images as input (a, b: training and testing test of modulus prediction; c, d: training and testing set of hardness prediction).

plex function space and the mapping function between the microstructure and the micromechanical properties can be found in this space by gradient descent to build a correlation. Overall, the advantage of Res-Net over the table model is that the Res-Net predicts based on detailed microstructural information, while the table model predicts based on a single greyscale value that represents the overall material composition.

However, some anomalous predictions can be observed. In Fig. 14, 12 randomly selected cases from the testing set are shown. Although the predictions of the Res-Net in most cases are close to the real values measured by nanoindentation, an anomalous prediction can still be found (as noted by the red-dash rectangle). The reason for such a discrepancy could be that the 2D BSE image does not fully represent the 3D microstructure probed by nanoindentation [62]. It is acknowledged that the backscattered electrons are emitted from a region that maybe shallower than the interaction volume under a nanoindenter tip. However, a BSE image in this case can act as a representative slice of a 3D structure. A CNN network may be able to infer certain microstructural information of the material near where the BSE image is taken. The results of the Res-Net indeed prove the effectiveness of BSE-based prediction.

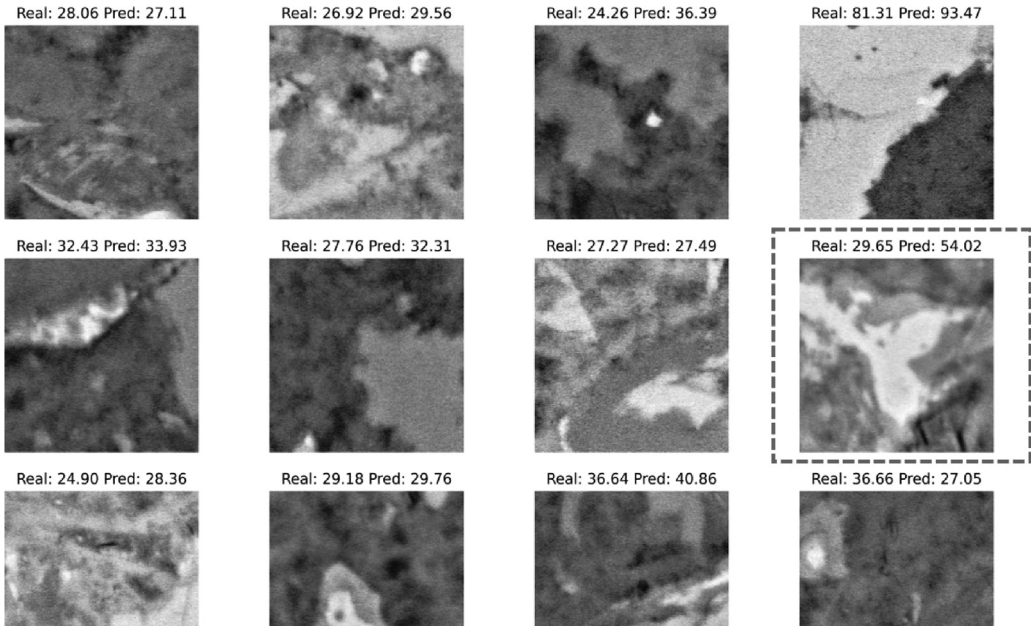

Fig. 14. Randomly selected cases of modulus prediction in the testing set.

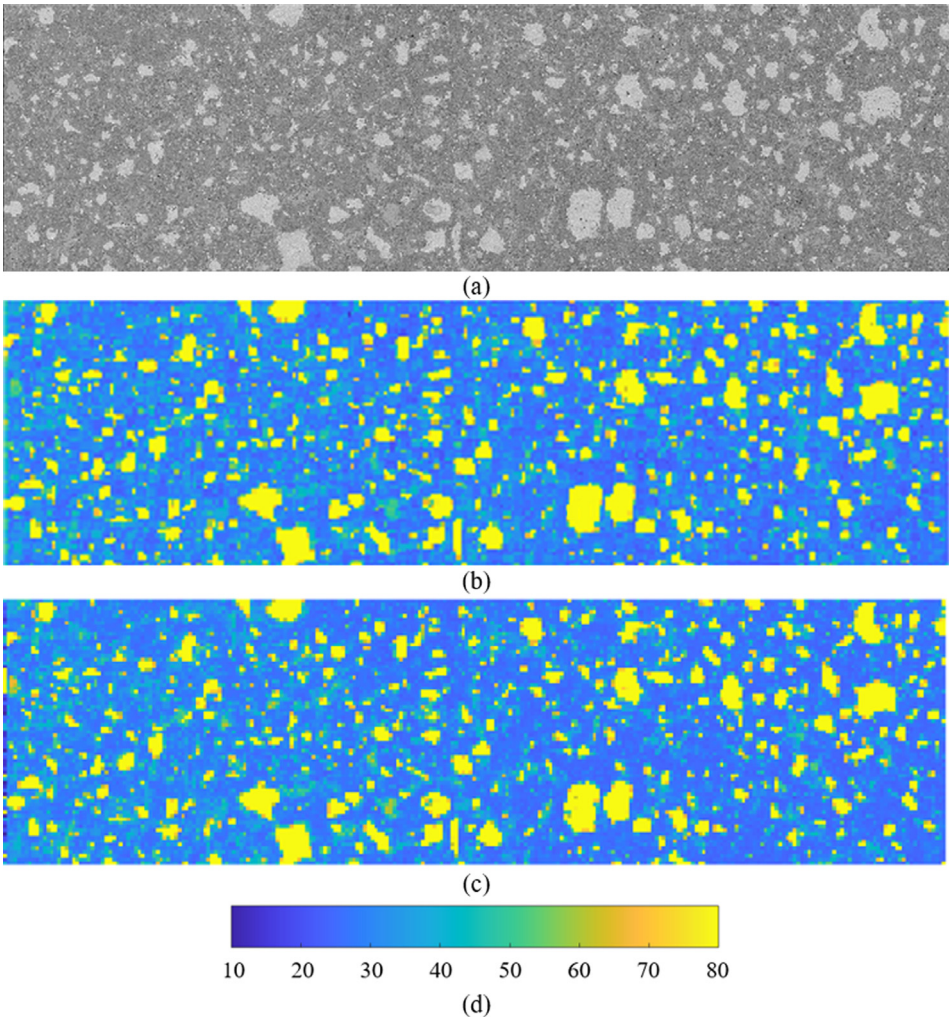

Fig. 15. Mapping the elastic modulus of a BSE image using RES-Net (a: BSE image of array A4; b: RES-Net mapping result; c: Table model mapping result; d: scale bar of the mapping result). Width of field = 2.6 mm.

5.4. Out-of-bag test

To further evaluate the applicability of the Res-Net, the area A4, where nano-indentation was never performed, was used for an out-of-bag test. The reason why the area A4 can be used for out-of-bag test is that, as shown in the section 5.1, when the number of indents increases, the deconvolution statistics including the fraction, mean and variance of each phase are invariant and indicate the inherent properties of the cement composite. Therefore, given an area that is large enough to represent the cement composite, if the prediction of the model over such an area follows the same statistics pattern, the applicability of the prediction model can be further validated. In the Fig. 15, the modulus mapping results by the Res-Net and the table model are presented. Both the Res-Net (Fig. 15b) and the table model (Fig. 15c) can correctly identify the yellow areas with a modulus over 80 GPa as the ACC, which is in good accordance with the BSE image (Fig. 15a).

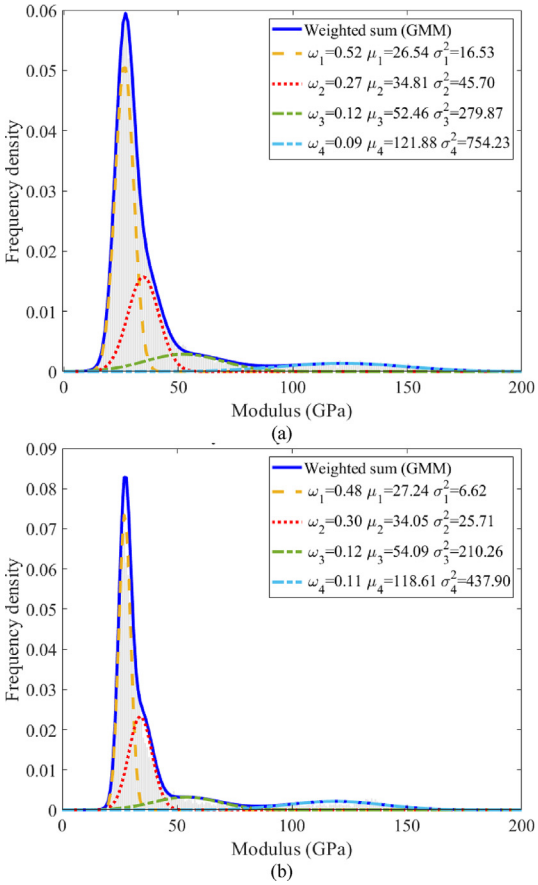

Fig. 16. Deconvolution of the mapping results of the RES-Net and table model (a: nanoindentation results on A3; b: RES-Net mapping result on A4; c: table model mapping result on A4).

The deconvolution results (see section 5.1) proves that invariant statistics of the four phases can be obtained even on different nanoindentation areas. Therefore, the prediction results of the table model and the Res-Net over an identical area should also obtain similar deconvolution statistics. In Fig. 16, the deconvolution results of nanoindentation test on the area A3 (20,000 indents) and the prediction results of Res-Net model and table model on the area A4 (18,907 indents) are presented. The reason why the results of area A3 was selected is because of its comparable size with the selected out-of-bag test area A4 and therefore can exclude the influence of data number on the deconvolution results. The result shows that the predictions of Res-Net can produce very close deconvolution statistics as the nanoindentation test, while the table model shows an obvious discrepancy in statistics of CH and ACC, as summarized in the Table. 1. The Res-Net obtained less variance than the test results in all phases, which indicates that the Res-Net trained based on the current dataset has not fully learned all features that needed to make perfect prediction of modulus based on microstructural input. In Fig. 17, the histogram of the aforementioned results shows that the Res-Net obtains closer results with the test, while the table model shows a much more obvious difference at the peak and a very unstable tail. The disturbance of the table model is attributed to its discontinuous nature, that each single average greyscale value corresponds to an average modulus. Nevertheless, the results of Res-Net shows discrepancy with the testing result, which may be explained by the following reasons: 1) limited dataset; 2) 2D BSE image does not reflect 3D microstructural information; 3) error in the micro-positioning procedure. Considering the relatively large size of the dataset in this study, potential improvement may be to 1) build the Res-Net based on 3D image (e.g, XCT); 2) improve the nano-indenter movement accuracy or build a more accurate error propagation model to compensate the error of nano-indenter movement.

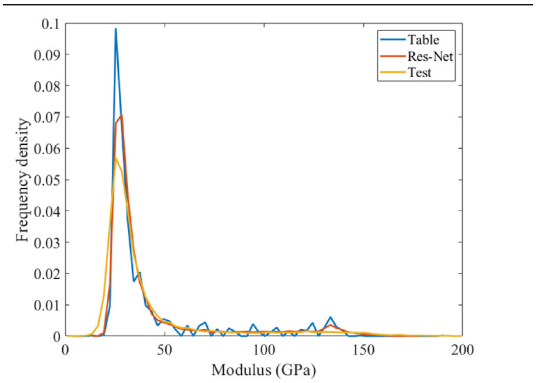

Fig. 17. Histogram of testing results A3 and prediction results of table model and Res-Net model.

Table 1
Comparison of the deconvolution statistics of tests, Res-Net prediction and table model prediction.

	Test A3		Res-Net		Table Model	
	Fraction	Range	Fraction	Range	Fraction	Range
LD	0.52	26.54 ± 4.06	0.48	27.24 ± 2.57	0.49	26.67 ± 1.86
HD	0.27	34.81 ± 6.76	0.30	34.05 ± 5.07	0.31	34.66 ± 5.82
CH	0.12	52.46 ± 16.73	0.12	54.09 ± 14.50	0.14	71.99 ± 27.11
ACC	0.09	121.88 ± 27.46	0.11	118.61 ± 20.93	0.06	130.23 ± 6.87

6. Conclusions

This paper implements computer vision technique to map the micromechanical properties of cement paste based on an input of BSE image. First, three prescribed areas were positioned, and BSE images of these areas were taken under a magnification of 5000X. By express nanoindentation tests, 40,000 indents were made to probe the micromechanical properties (*i.e.*, elastic modulus and hardness) of the prescribed areas. Accordingly, 40,000 10 × 10 μm^2 BSE images corresponding to each indent were cropped by a micro-positioning procedure. The dataset containing 40,000 BSE images and corresponding micromechanical properties was then used to train a Res-Net model which was featured by a shortcut connection comparing to typical CNN architecture. The following conclusions can be drawn:

1) For ordinary Portland cement, assuming four phases are present (*i.e.*, LD-CSH, HD-CSH, CH and ACC), GMM deconvolution of our express nanoindentation test results can obtain almost invariant statistics (*i.e.*, fraction, mean and standard deviation) for each phase, provided that over 20,000 samples are available for the deconvolution fitting. Smaller sample size may lead to slightly unstable results.
2) A positive correlation exists between the average greyscale value of the BSE image and elastic modulus. A table model trained on a training set of 32,000 data can predict the elastic modulus and hardness over a testing set of 8,000 data with a R^2 of 0.80 and 0.83.
3) With 70%, 15% and 15% of 40,000 data points in training, validation, and testing set respectively, the trained Res-Net is able to reliably predict the elastic modulus and hardness from a 10 × 10 μm^2 BSE image. The hardness prediction of Res-Net on testing set are quantified by a MAE of 0.30 GPa and a R^2 of 0.88. The modulus prediction of Res-Net on testing set are quantified by a MAE of 6.40 GPa and a R^2 of 0.85, both of which show advantage over the table model.
4) In the out-of-bag test, the Res-Net can produce modulus mapping that is highly correlated to the BSE image. As a comparison, the prediction made by the table model shows obvious deviation in histogram and deconvolution statistics of CH and ACC. The GMM deconvolution of the Res-Net prediction over 18,907 10 × 10 μm^2 areas obtains similar invariant statistics derived by the nanoindentation tests containing 20,000 indents, which gives strong evidence of the applicability of the Res-Net model.

The proposed Res-Net for predicting the micromechanical properties of cement paste is a promising approach to overcome the four-phase assumption that is commonly used in many SNI studies and multiscale modelling of cementitious materials, since it can generate micromechanical mapping with a high resolution. Limitations regarding the prediction accuracy still exist. Further studies should focus on 3D-CNN model which takes 3D images (*e.g.*, XCT) rather than 2D BSE images as training data.

On the other hand, the techniques discussed in the study are important if we move to more sustainable concretes, using different binders (*e.g.*, supplementary cementitious materials or alkali activated materials) and aggregates (*e.g.*, recycled aggregates or waste materials). The microstructures will have different properties and behaviour compared to concretes based on OPC and natural aggregates. Nano-indentation combined with computer vision can measure and predict the changes on the micro-level, which is then an input for models that predict the behaviour of the sustainable concretes.

Data availability

Data will be made available on request.

Declaration of Competing Interest

The authors declare that they have no known competing financial interests or personal relationships that could have appeared to influence the work reported in this paper.

Acknowledgements

Minfei Liang, Yidong Gan, and Ze Chang would like to acknowledge the funding supported by China Scholarship Council under grant number 202007000027, 201706130140, and 201806060129. Branko Šavija acknowledges the financial support of the European Research Council (ERC) within the framework of the ERC Starting Grant Project "Auxetic Cementitious Composites by 3D printing (ACC-3D)", Grant Agreement Number 101041342. Hongzhi Zhang acknowledges the financial support of the National Natural Science Foundation of China (No.52008234) and Natural Science Foundation of Jiangsu Province (No. BK20200235).

Shan He acknowledges the financial supports from the MSCA-ITN SMARTINCS project. The project has received funding from the European Union's Horizon 2020 research and innovation programme under the Marie Skłodowska-Curie grant agreement No 860006.

References

[1] H. Zhang, Y. Xu, Y. Gan, Z. Chang, E. Schlangen, B. Šavija, Microstructure informed micromechanical modelling of hydrated cement paste: Techniques and challenges, Constr. Build. Mater. 251 (2020), https://doi.org/10.1016/J.CONBUILDMAT.2020.118983 118983.
[2] E. Schlangen, E.J. Garboczi, Fracture simulations of concrete using lattice models: Computational aspects, Eng. Fract. Mech. 57 (1997) 319–332, https://doi.org/10.1016/S0013-7944(97)00010-6.
[3] H. Zhang, Y. Xu, Y. Gan, Z. Chang, E. Schlangen, B. Šavija, Combined experimental and numerical study of uniaxial compression failure of hardened cement paste at micrometre length scale, Cem. Concr. Res. 126 (2019), https://doi.org/10.1016/J.CEMCONRES.2019.105925 105925.
[4] H. Zhang, B. Šavija, S.C. Figueiredo, E. Schlangen, Experimentally validated multi-scale modelling scheme of deformation and fracture of cement paste, Cem. Concr. Res. 102 (2017) 175–186, https://doi.org/10.1016/J.CEMCONRES.2017.09.011.
[5] H. Zhang, B. Šavija, Y. Xu, E. Schlangen, Size effect on splitting strength of hardened cement paste: Experimental and numerical study, Cem. Concr. Compos. 94 (2018) 264–276, https://doi.org/10.1016/J.CEMCONCOMP.2018.09.018.
[6] Y. Gan, C. Romero Rodriguez, H. Zhang, E. Schlangen, K. Breugel, B. Šavija, Modeling of microstructural effects on the creep of hardened cement paste using an experimentally informed lattice model, Comput. Aided Civ. Inf. Eng. 36 (2021) 560–576, https://doi.org/10.1111/mice.12659.
[7] P. Gao, G. Ye, H. Huang, Z. Qian, E. Schlangen, J. Wei, Q. Yu, Incorporating elastic and creep deformations in modelling the three-dimensional autogenous shrinkage of cement paste, Cem. Concr. Res. 160 (2022), https://doi.org/10.1016/J.CEMCONRES.2022.106907 106907.
[8] Y. Gan, H. Zhang, M. Liang, E. Schlangen, K. van Breugel, B. Šavija, A numerical study of fatigue of hardened cement paste at the microscale, Int. J. Fatigue 151 (2021), https://doi.org/10.1016/J.IJFATIGUE.2021.106401 106401.
[9] T. Mori, K. Tanaka, Average stress in matrix and average elastic energy of materials with misfitting inclusions, Acta Metall. 21 (1973) 571–574, https://doi.org/10.1016/0001-6160(73)90064-3.
[10] R. Hill, A self-consistent mechanics of composite materials, J. Mech. Phys. Solids 13 (1965) 213–222, https://doi.org/10.1016/0022-5096(65)90010-4.
[11] G. Constantinides, F.J. Ulm, The effect of two types of C-S-H on the elasticity of cement-based materials: Results from nanoindentation and micromechanical modeling, Cem. Concr. Res. 34 (2004) 67–80, https://doi.org/10.1016/S0008-8846(03)00230-8.

[12] O. Bernard, F.-J. Ulm, E. Lemarchand, A multiscale micromechanics-hydration model for the early-age elastic properties of cement-based materials, Cem. Concr. Res. 33 (2003) 1293–1309, https://doi.org/10.1016/S0008-8846(03)00039-5.
[13] S. Liang, Y. Wei, Z. Wu, Multiscale modeling elastic properties of cement-based materials considering imperfect interface effect, Constr. Build. Mater. 154 (2017) 567–579, https://doi.org/10.1016/j.conbuildmat.2017.07.196.
[14] M. Vandamme, F.-J. Ulm, Nanoindentation investigation of creep properties of calcium silicate hydrates, Cem. Concr. Res. 52 (2013) 38–52, https://doi.org/10.1016/j.cemconres.2013.05.006.
[15] Y. Li, Y. Liu, Y. Li, Y. Li, R. Wang, Evaluation of concrete creep properties based on indentation test and multiscale homogenization method, Cem. Concr. Compos. 123 (2021), https://doi.org/10.1016/J.CEMCONCOMP.2021.104135 104135.
[16] L. Sorelli, G. Constantinides, F.J. Ulm, F. Toutlemonde, The nano-mechanical signature of Ultra High Performance Concrete by statistical nanoindentation techniques, Cem. Concr. Res. 38 (2008) 1447–1456, https://doi.org/10.1016/J.CEMCONRES.2008.09.002.
[17] C. Hu, Z. Li, Micromechanical investigation of Portland cement paste, Constr. Build. Mater. 71 (2014) 44–52, https://doi.org/10.1016/j.conbuildmat.2014.08.017.
[18] W.R.L. da Silva, J. Němeček, P. Štemberk, Methodology for nanoindentation-assisted prediction of macroscale elastic properties of high performance cementitious composites, Cem. Concr. Compos. 45 (2014) 57–68, https://doi.org/10.1016/J.CEMCONCOMP.2013.09.013.
[19] W. Wilson, L. Sorelli, A. Tagnit-Hamou, Unveiling micro-chemo-mechanical properties of C-(A)-S-H and other phases in blended-cement pastes, Cem. Concr. Res. 107 (2018) 317–336, https://doi.org/10.1016/J.CEMCONRES.2018.02.010.
[20] L. Göbel, C. Bos, R. Schwaiger, A. Flohr, A. Osburg, Micromechanics-based investigation of the elastic properties of polymer-modified cementitious materials using nanoindentation and semi-analytical modeling, Cem. Concr. Compos. 88 (2018) 100–114, https://doi.org/10.1016/j.cemconcomp.2018.01.010.
[21] G. Fang, Q. Wang, M. Zhang, Micromechanical analysis of interfacial transition zone in alkali-activated fly ash-slag concrete, Cem. Concr. Compos. 119 (2021), https://doi.org/10.1016/j.cemconcomp.2021.103990 103990.
[22] Z. Luo, W. Li, Y. Gan, X. He, A. Castel, D. Sheng, Nanoindentation on micromechanical properties and microstructure of geopolymer with nano-SiO2 and nano-TiO2, Cem. Concr. Compos. 117 (2021), https://doi.org/10.1016/j.cemconcomp.2020.103883.
[23] Y. Sun, J.-X. Lu, C.S. Poon, Strength degradation of seawater-mixed alite pastes: an explanation from statistical nanoindentation perspective, Cem. Concr. Res. 152 (2022), https://doi.org/10.1016/j.cemconres.2021.106669 106669.
[24] W. Wilson, J.M. Rivera-Torres, L. Sorelli, A. Durán-Herrera, A. Tagnit-Hamou, The micromechanical signature of high-volume natural pozzolan concrete by combined statistical nanoindentation and SEM-EDS analyses, Cem. Concr. Res. 91 (2017) 1–12, https://doi.org/10.1016/J.CEMCONRES.2016.10.004.
[25] Y. Wei, S. Liang, X. Gao, Indentation creep of cementitious materials: Experimental investigation from nano to micro length scales, Constr. Build. Mater. 143 (2017) 222–233, https://doi.org/10.1016/j.conbuildmat.2017.03.126.
[26] Z. Hu, M. Wyrzykowski, M. Griffa, K. Scrivener, P. Lura, Young's modulus and creep of calcium-silicate-hydrate compacts measured by microindentation, Cem. Concr. Res. 134 (2020), https://doi.org/10.1016/j.cemconres.2020.106104.
[27] P. Lura, P. Trtik, B. Münch, Validity of recent approaches for statistical nanoindentation of cement pastes, Cem. Concr. Compos. 33 (2011) 457–465, https://doi.org/10.1016/J.CEMCONCOMP.2011.01.006.
[28] P. Trtik, B. Münch, P. Lura, A critical examination of statistical nanoindentation on model materials and hardened cement pastes based on virtual experiments, Cem. Concr. Compos. 31 (2009) 705–714, https://doi.org/10.1016/J.CEMCONCOMP.2009.07.001.
[29] C. Hu, Y. Gao, Y. Zhang, Z. Li, Statistical nanoindentation technique in application to hardened cement pastes: Influences of material microstructure and analysis method, Constr. Build. Mater. 113 (2016) 306–316, https://doi.org/10.1016/j.conbuildmat.2016.03.064.
[30] H. Zhang, B. Šavija, M. Luković, E. Schlangen, Experimentally informed micromechanical modelling of cement paste: An approach coupling X-ray computed tomography and statistical nanoindentation, Compos. B Eng. 157 (2019) 109–122, https://doi.org/10.1016/J.COMPOSITESB.2018.08.102.
[31] B. Šavija, H. Zhang, E. Schlangen, Micromechanical testing and modelling of blast furnace slag cement pastes, Constr. Build. Mater. 239 (2020), https://doi.org/10.1016/j.conbuildmat.2019.117841.
[32] D.H. Phillips, J.J. Lannutti, Measuring physical density with X-ray computed tomography, NDT and E Int. 30 (1997) 339–350, https://doi.org/10.1016/S0963-8695(97)00020-0.
[33] N. Douarche, D. Rouby, G. Peix, J.M. Jouin, Relations between X-ray tomography, density and mechanical properties in carbon-carbon composites, Carbon N Y. 39 (2001) 1455–1465, https://doi.org/10.1016/S0008-6223(00)00196-2.
[34] K. Scrivener, R. Snellings, B. Lothenbach, A practical guide to microstructural analysis of cementitious materials, n.d.
[35] Y. Ren, J. Huang, Z. Hong, W. Lu, J. Yin, L. Zou, X. Shen, Image-based concrete crack detection in tunnels using deep fully convolutional networks, Constr. Build. Mater. 234 (2020), https://doi.org/10.1016/J.CONBUILDMAT.2019.117367 117367.
[36] J. Liu, X. Yang, S. Lau, X. Wang, S. Luo, V.C. Lee, L. Ding, Automated pavement crack detection and segmentation based on two-step convolutional neural network, Computer-Aided Civil and Infrastructure, Engineering 35 (2020) 1291–1305, https://doi.org/10.1111/mice.12622.
[37] M. Flah, A.R. Suleiman, M.L. Nehdi, Classification and quantification of cracks in concrete structures using deep learning image-based techniques, Cem. Concr. Compos. 114 (2020), https://doi.org/10.1016/J.CEMCONCOMP.2020.103781 103781.
[38] C.V. Dung, L.D. Anh, Autonomous concrete crack detection using deep fully convolutional neural network, Autom. Constr. 99 (2019) 52–58, https://doi.org/10.1016/J.AUTCON.2018.11.028.
[39] M. Azimi, G. Pekcan, Structural health monitoring using extremely compressed data through deep learning, Computer-Aided Civil and Infrastructure, Engineering 35 (2020) 597–614, https://doi.org/10.1111/mice.12517.
[40] B.K. Oh, B. Glisic, Y. Kim, H.S. Park, Convolutional neural network-based wind-induced response estimation model for tall buildings, Computer-Aided Civil and Infrastructure, Engineering 34 (2019) 843–858, https://doi.org/10.1111/mice.12476.
[41] X. Liang, Image-based post-disaster inspection of reinforced concrete bridge systems using deep learning with Bayesian optimization, Computer-Aided Civil and Infrastructure, Engineering 34 (2019) 415–430, https://doi.org/10.1111/mice.12425.
[42] C. Yang, Y. Kim, S. Ryu, G.X. Gu, Prediction of composite microstructure stress-strain curves using convolutional neural networks, Mater. Des. 189 (2020), https://doi.org/10.1016/J.MATDES.2020.108509 108509.
[43] C. Rao, Y. Liu, Three-dimensional convolutional neural network (3D-CNN) for heterogeneous material homogenization, Comput. Mater. Sci 184 (2020), https://doi.org/10.1016/J.COMMATSCI.2020.109850 109850.
[44] M. Liang, Y. Gan, Z. Chang, Z. Wan, E. Schlangen, B. Šavija, Microstructure-informed deep convolutional neural network for predicting short-term creep modulus of cement paste, Cem. Concr. Res. 152 (2022), https://doi.org/10.1016/J.CEMCONRES.2021.106681 106681.
[45] B. Hilloulin, I. Bekrine, E. Schmitt, A. Loukili, Open-source deep learning-based air-void detection algorithm for concrete microscopic images, J. Microsc. 286 (2022) 179–184, https://doi.org/10.1111/jmi.13098.
[46] B. Hilloulin, I. Bekrine, E. Schmitt, A. Loukili, Modular deep learning segmentation algorithm for concrete microscopic images, Constr. Build. Mater. 349 (2022), https://doi.org/10.1016/J.CONBUILDMAT.2022.128736 128736.
[47] J. Zhang, G.W. Scherer, Comparison of methods for arresting hydration of cement, Cem. Concr. Res. 41 (2011) 1024–1036, https://doi.org/10.1016/J.CEMCONRES.2011.06.003.
[48] M. Miller, C. Bobko, M. Vandamme, F.J. Ulm, Surface roughness criteria for cement paste nanoindentation, Cem. Concr. Res. 38 (2008) 467–476, https://doi.org/10.1016/J.CEMCONRES.2007.11.014.
[49] M. Sebastiani, R. Moscatelli, F. Ridi, P. Baglioni, F. Carassiti, High-resolution high-speed nanoindentation mapping of cement pastes: Unravelling the effect of microstructure on the mechanical properties of hydrated phases, Mater. Des. 97 (2016) 372–380, https://doi.org/10.1016/j.matdes.2016.02.087.
[50] W.C. Oliver, G.M. Pharr, An improved technique for determining hardness and elastic modulus using load and displacement sensing indentation experiments, J. Mater. Res. 7 (1992) 1564–1583, https://doi.org/10.1557/jmr.1992.1564.
[51] S. Khan, H. Rahmani, S.A.A. Shah, M. Bennamoun, A Guide to Convolutional Neural Networks for Computer Vision, Synthesis Lectures on Computer Vision. 8 (2018) 1–207, https://doi.org/10.2200/S00822ED1V01Y201712COV015.
[52] I. Goodfellow, Y. Bengio, A. Courville, Deep Learning, MIT Press, 2016.
[53] J.T. Springenberg, A. Dosovitskiy, T. Brox, M. Riedmiller, Striving for Simplicity: The All Convolutional Net, (2014).
[54] K. He, X. Zhang, S. Ren, J. Sun, Deep Residual Learning for Image Recognition, (2015).
[55] D.P. Kingma, J. Ba, Adam: A Method for Stochastic Optimization, (2014).
[56] D. Davydov, M. Jirásek, L. Kopecký, Critical aspects of nano-indentation technique in application to hardened cement paste, Cem. Concr. Res. 41 (2011) 20–29, https://doi.org/10.1016/J.CEMCONRES.2010.09.001.
[57] C. Hu, Z. Li, A review on the mechanical properties of cement-based materials measured by nanoindentation, Constr. Build. Mater. 90 (2015) 80–90, https://doi.org/10.1016/j.conbuildmat.2015.05.008.
[58] P.D. Tennis, H.M. Jennings, A model for two types of calcium silicate hydrate in the microstructure of Portland cement pastes, Cem. Concr. Res. 30 (2000) 855–863, https://doi.org/10.1016/S0008-8846(00)00257-X.
[59] K. van Breugel, Simulation of hydration and formation of structure in hardening cement-based materials, Delft University of Technology, 1993.
[60] J. Li, W. Zhang, P.J.M. Monteiro, Preferred orientation of calcium aluminosilicate hydrate compacts: Implications for creep and indentation, Cem. Concr. Res. 143 (2021), https://doi.org/10.1016/J.CEMCONRES.2021.106371 106371.
[61] F. Pedregosa, G. Varoquaux, A. Gramfort, V. Michel, B. Thirion, O. Grisel, M. Blondel, A. Müller, J. Nothman, G. Louppe, P. Prettenhofer, R. Weiss, V. Dubourg, J. Vanderplas, A. Passos, D. Cournapeau, M. Brucher, M. Perrot É., Duchesnay, Machine Learning in Python, Scikit-learn, 2012.
[62] M. Luković, E. Schlangen, G. Ye, Combined experimental and numerical study of fracture behaviour of cement paste at the microlevel, Cem. Concr. Res. 73 (2015) 123–135, https://doi.org/10.1016/J.CEMCONRES.2015.03.008.